The Performance of Four Spectral GCMs in the Southern Hemisphere: The January and July Climatology and the Semiannual Wave

JIN-SONG XU AND HANS VON STORCH*

Max-Planck-Institut für Meteorologie, Hamburg, Federal Republic of Germany

HARRY VAN LOON†

National Center for Atmospheric Research, Boulder, Colorado

(Manuscript received 28 December 1988, in final form 10 August 1989)

ABSTRACT

Monthly mean sea level pressure (SLP) data from four low-resolution spectral GCMs—ECMWF T21, CCC, NCAR CCM and GFDL R15—are compared with observations for the Southern Hemisphere.

Characteristics of the observed Southern Hemisphere January and July mean mass distribution are:

(i) high pressure areas in the subtropics;
(ii) a steep meridional gradient at midlatitudes;
(iii) a circumpolar trough in the Antarctic;
(iv) a zonal asymmetry dominated by zonal wave 1, which has an almost complete phase reversal near 40°S;
(v) a double westerly wind maximum during the colder part of the year.

The CCC model reproduces some of these features. The ECMWF model, the NCAR CCM, and the GFDL models fail with respect to (ii) and (iii). All GCMs underestimate the intensity of the stationary eddies. None of the models considered reproduces the double westerly wind maximum.

Another marked feature of the Southern Hemisphere circulation is the semiannual wave that dominates the annual curve of SLP at mid- and polar latitudes. Regardless of the various models' degree of success in reproducing the mean circulation, all fail in simulating the general features of the semiannual wave.

1. Introduction

The Southern Hemisphere circulation is characterized by a few unique features; i.e., the polar jet stream, the zonal asymmetries, the double jet-stream in the colder part of the year, and the dominant semiannual wave in middle and high latitudes. In this paper we examine present state-of-the-art general circulation models (GCMs) that have been used extensively for climate simulation and sensitivity studies to see if they are able to reproduce these Southern Hemisphere features.

Few studies of the ability of GCMs to reproduce the Southern Hemisphere climatology have been published. Schlesinger (1984a,b) examined the summer and winter climates in the Southern Hemisphere as simulated by six global GCMs—the grid point models used at Goddard Institute for Space Studies (GISS), Goddard Laboratory for Atmospheric Sciences (GLAS), Oregon State University (OSU), and the University of California Los Angeles (UCLA); and the spectral models of the National Center for Atmospheric Research (NCAR) and Geophysical Fluid Dynamics Laboratory (GFDL). January and July means, simulated by the Japanese Meteorological Research Institute (MRI) GCM in the annual cycle mode, are presented by Tokioka et al. (1985) and Kitoh and Tokioka (1986). The performance of the Australian Bureau of Meteorological Research (BMRC) model has been documented by Hart et al. (1988). Storch and Xu (1987) considered the ability of the ECMWF T21 model to reproduce the extratropical semiannual wave. They found that the ECMWF model simulates a wave that is too weak and differs from the observations with respect to its amplitude and phase (Van Loon 1967, 1972, 1984). Similar results were obtained by Weickmann and Chervin (1988), who considered tropospheric winds simulated by the NCAR CCM. In this paper we extend the Storch and Xu (1987) study to include three additional spectral models and present

* Scientific visitor at NCAR.
† NCAR is sponsored by the National Science Foundation.

Corresponding author address: Jin-Song Xu, Max Planck Institut fur Meteorologie, Bundesstrasse 55, D-2000 Hamburg 13, Federal Republic of Germany.

results on Southern Hemisphere sea level pressure (SLP), 500-mb height, and 500-mb temperature.

The purpose of this paper is to describe the models' ability to reproduce the Southern Hemisphere circulation and not to find out why the models fail to reproduce certain aspects of the circulation. Also, we do not intend to discover why the models behave differently from each other. It is well known among GCM users that it is generally impossible to trace a model's insufficiency to an inadequate formulation of either the numerics or the parameterization of a single physical process.

The data are described in section 2. In section 3, the GCM-generated and the observed circulation in January and July are compared: the mean mass distributions in section 3.1, the stationary 500-mb height waves in section 3.2, and the meridional gradient of tropospheric temperature in section 3.3. The semiannual wave in SLP, and 500-mb temperature gradient in the models and in the observed data is considered in section 4. A summary and discussion are given in section 5.

2. Data

The long-term means of observed data have been calculated for each month using daily analyses compiled by the South African Weather Bureau (SLP, January 1951–December 1958, 500 mb height, July 1957–December 1958), and by the Australian. Bureau of Meteorology (SLP, 500 mb height and temperature, May 1972–August 1983).

The GCM data are from extended integrations performed with four spectral GCMs of similar horizontal and vertical resolution:

1) a 20-year run performed with the T20 model of the Canadian Climate Center (henceforth referred to as the CCC model; Boer et al. 1984),

2) a 3-year run of the NCAR Community Climate Model [NCAR CCM, Washington and Meehl (1984); Meehl (1989)],

3) a 15-year run of the GFDL R15 model [GFDL model, Manabe and Hahn (1981)],

4) a 10-year run of the ECMWF T21 model installed in Hamburg [ECMWF model; Fischer (1987)].

The four models all use climatological sea surface temperature. The main characteristics of the models' designs are listed in Table 1.

In the following, we regard sample means as being identical to the unknown ensemble means; e.g., we assume that the mean January SLP field is identical to the average of all available observed January fields, and consider the characteristics of the semiannual wave that are derived from the available finite sample to be unaffected by the interannual variability of monthly mean fields. Storch and Xu (1987) took the uncertainty stemming from interannual variability into account and used multivariate tests to compare observed and simulated mean fields. We found that almost all differences between the GCM and the observed fields were significantly nonzero with a risk well below 1%. If we applied, the same statistical procedure to the GCM data in this study, similarly small risks would be obtained.

The GFDL model output has previously been examined by Manabe and Hahn (1981) and by Schlesinger (1983a,b). The model sea level pressure distributions shown in these papers deviate slightly from those shown in the present paper since we inferred SLP from 1000 mb height and zonally averaged surface temperature. The NCAR model output considered by Schlesinger (1984a,b) stems from perpetual January and July integrations, whereas we are considering a multiyear integration.

3. Mean SLP, 500-mb height and 500-mb meridional temperature gradient in January and in July

a. Monthly mean fields

The monthly mean SLP and 500-mb geopotential height fields for January and July are shown in Figs. 1–4. The zonal mean latitudinal position and the strength of the subpolar trough in January and July may be derived from Fig. 15, which shows the annual cycle of these quantities.

1) MEAN SEA LEVEL PRESSURE: JANUARY

The observed mean January SLP field has a subtropical ridge with centers in the eastern part of the oceans and a steep midlatitude slope to a circumpolar trough near 65°S.

The CCC model produces a realistic midlatitude pressure gradient (Boer et al., 1984). The position and intensity of the subtropical highs are quite well simulated. The subpolar trough lies a few degrees too far south.

In the NCAR CCM the pressure in the subtropical highs is about 4 mb higher and in the subpolar trough about 10 mb higher than in the observations, which results in a weak meridional pressure gradient. The subtropical highs are situated in the eastern part of each ocean as in the observations, whereas the subpolar trough lies too far north.

In the GFDL model the locations of the subtropical highs are correctly simulated, but their strength is somewhat overestimated. On the other hand, the pressure in the subpolar trough is too high, by about 20 mb, so that the meridional pressure gradient is too weak. The trough also lies too far north.

In the ECMWF model the subtropical ridge is correctly located but about 10 mb too weak. The subpolar trough is not deep enough, and the observed strong midlatitude zonal circulation is thus poorly simulated. The unrealistic ridge found in the subpolar Pacific Ocean is due to an inconsistent numerical discretization (Simmons 1989, personal communication).

TABLE 1. Characteristics of the four low-resolution spectral GCMs examined in this study: Canadian Climate Centre (CCC), National Center for Atmospheric Research (NCAR), Geophysical Fluid Dynamics Laboratory (GFDL) and European Centre for Medium Range Weather Forecasts (ECMWF).

	CCC	NCAR	GFDL	ECMWF
independent variables	λ, ϕ, σ, t	λ, ϕ, σ, t	λ, ϕ, σ, t	λ, ϕ, η, t
dependent variables	$\Phi, \zeta, D, T - T_d, \ln p_s$	$\zeta, D, T, q, \ln p_s$	Ψ, χ, T, q, p_s	$\zeta, D, T, q, \ln p_s$
resolution	triang. T20	rhomb. R15	rhomb. R15	triang. T21
$\Delta\lambda, \Delta\phi$	5.6°, 5.6°	4.5°, 7.5°	4.5°, 7.5°	5.6°, 5,6°
vertical	10 unevenly spaced levels	9 unevenly spaced levels	9 unevenly spaced levels	16 unevenly spaced levels
vertical finite diff. scheme	2nd order accuracy	energy and enstrophy conserving	2nd order accuracy	energy and enstrophy conserving
vertical boundary cond.	$\dot{\sigma} = 0$ at $p = p_s$ and $p = 0$	$\dot{\sigma} = 0$ at $p = p_s$ and $p = 0$	$\dot{\sigma} = 0$ at $p = p_s$ and $p = 0$	$\dot{\eta} = 0$ at $p = p_s$ and $p = 0$
time integration	leapfrog semi-implicit	leapfrog semi-implicit	leapfrog semi-implicit	leapfrog semi-implicit
Δt	30 min	40 min	30 min	45 min
horizontal diffusion	scale depend.	linear 2nd order	linear, 4th order	linear, 4th order
earth surface				
specified	background albedo, roughness, sea ice, SST	albedo, roughness, sea ice, SST	albedo, roughness, sea ice, SST	albedo, roughness, sea ice, SST, deep soil moisture and temperature
computed	albedo, snow, soil moisture and temperature	snow, soil moisture and temperature	snow, soil moisture and temperature	snow, soil moisture and temperature, albedo over snow
orography	truncated at T20 from high resolut. data	truncated at R15 from high resolut. data spectr. fitted	truncated at R15 from high resolut. data smoothed	truncated at T21 from high resolut. data spectr. fitted
physical parameterization				
boundary layer	turbulent fluxes depd. on roughness length and local stabil.	Prandtl layer approximation	height dependt. mixing length no stability dependence	turbulent fluxes depd. on roughness length and local stability
free atmosphere diffusion	depd. on mix. length and Richardson n.	depd. on mix. length and wind shear	no vertical diffusion for $\sigma < 0.68$	depd. on mix. length and Richardson n.
convection	"soft" convective ad.	moist convective ad.	moist convective ad.	Kuo (1974) scheme
clouds	specified	predicted	specified	predicted
mountain gravity wave drag	yes	no	no	no
reference	Boer et al. 1984	Washington and Meehl 1984 Meehl 1989	Manabe and Hahn 1981 Gordon and Stern 1982	Fischer 1987

2) MEAN SEA LEVEL PRESSURE: JULY

In the observations the subtropical ridge intensifies and shifts northward from summer to winter. The subpolar trough in July is similar to that in January. At 40°S–60°S the meridional gradient is about the same as in January over the Atlantic and Indian ocean, but in the Pacific it is distinctly weaker. A three-wave pattern is found at higher latitudes.

In the NCAR CCM and the GFDL and ECMWF models the subtropical highs intensify from summer to winter. The NCAR CCM simulates an anticyclone over South America instead of an anticyclone over each of the adjacent oceans. The intensities of the highs are overestimated by the NCAR and the GFDL models, and underestimated by the ECMWF model. In all three the subpolar trough is too weak and situated farther north than observed, and the midlatitude gradients are poorly simulated, especially in the ECMWF model. The very high pressure over Antarctica is probably a spurious effect of the reduction to sea level. The CCC model does well, but lacks a separate high above 1020 mb in the eastern Pacific.

3) MEAN 500-MB GEOPOTENTIAL HEIGHT: JANUARY

The observed field (Fig. 3) has a nearly zonally symmetric structure, deformed mainly by a wave 1. The strength of the zonally symmetric component may conveniently be measured by the zonally averaged height difference between 40°S and 60°S, which is about 44 gpdam. The zonal asymmetry appears as a

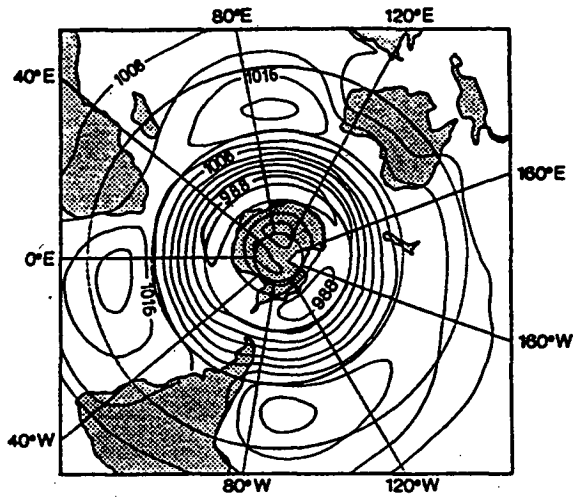

FIG. 1. January monthly mean SLP fields as observed and as simulated by the NCAR, the CCC, the GFDL and the ECMWF models. Note that the subtropical 1016 mb line in the GFDL and NCAR model data coincides with the 1012 mb line in the observations. (Units: mb; spacing: 4 mb.)

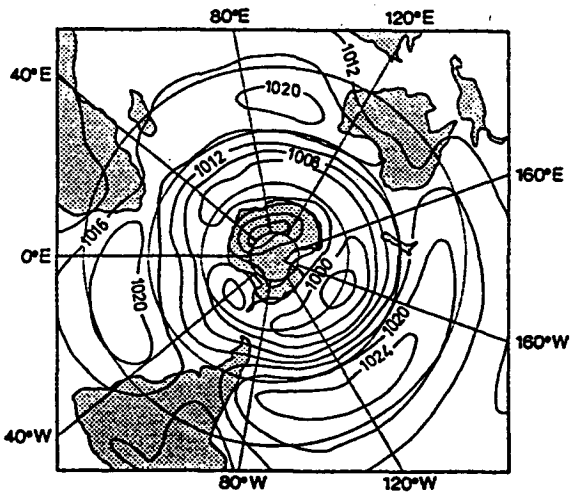

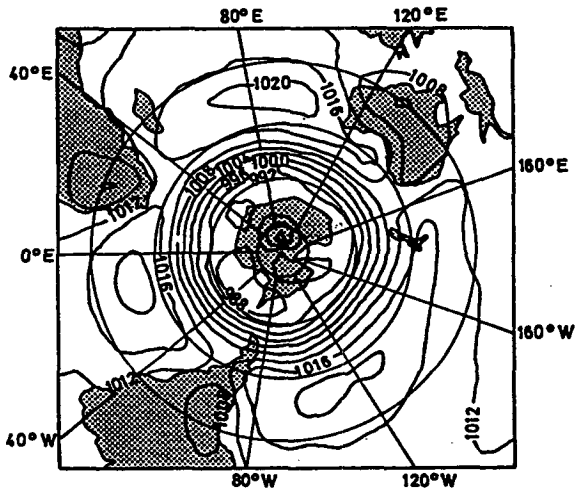

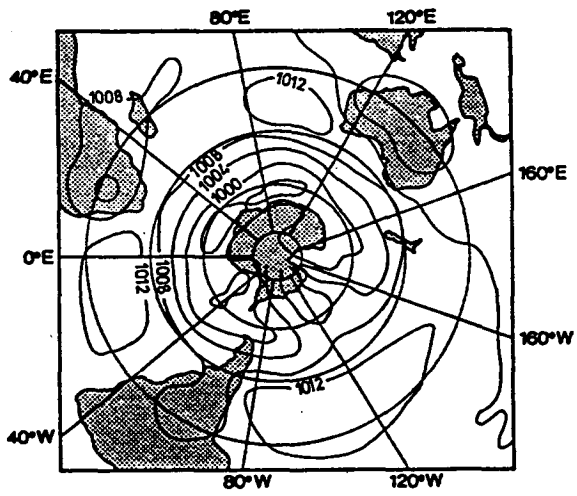

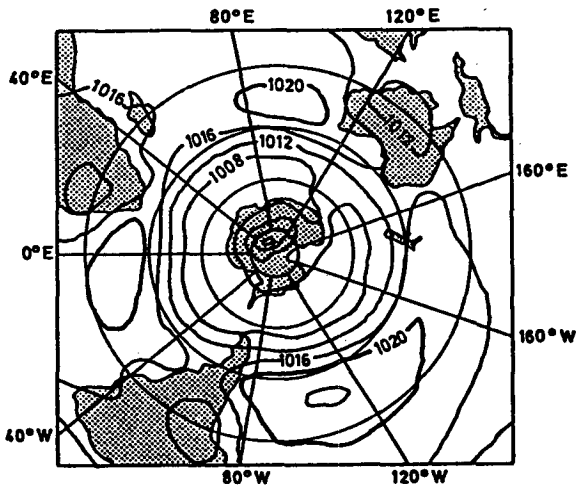

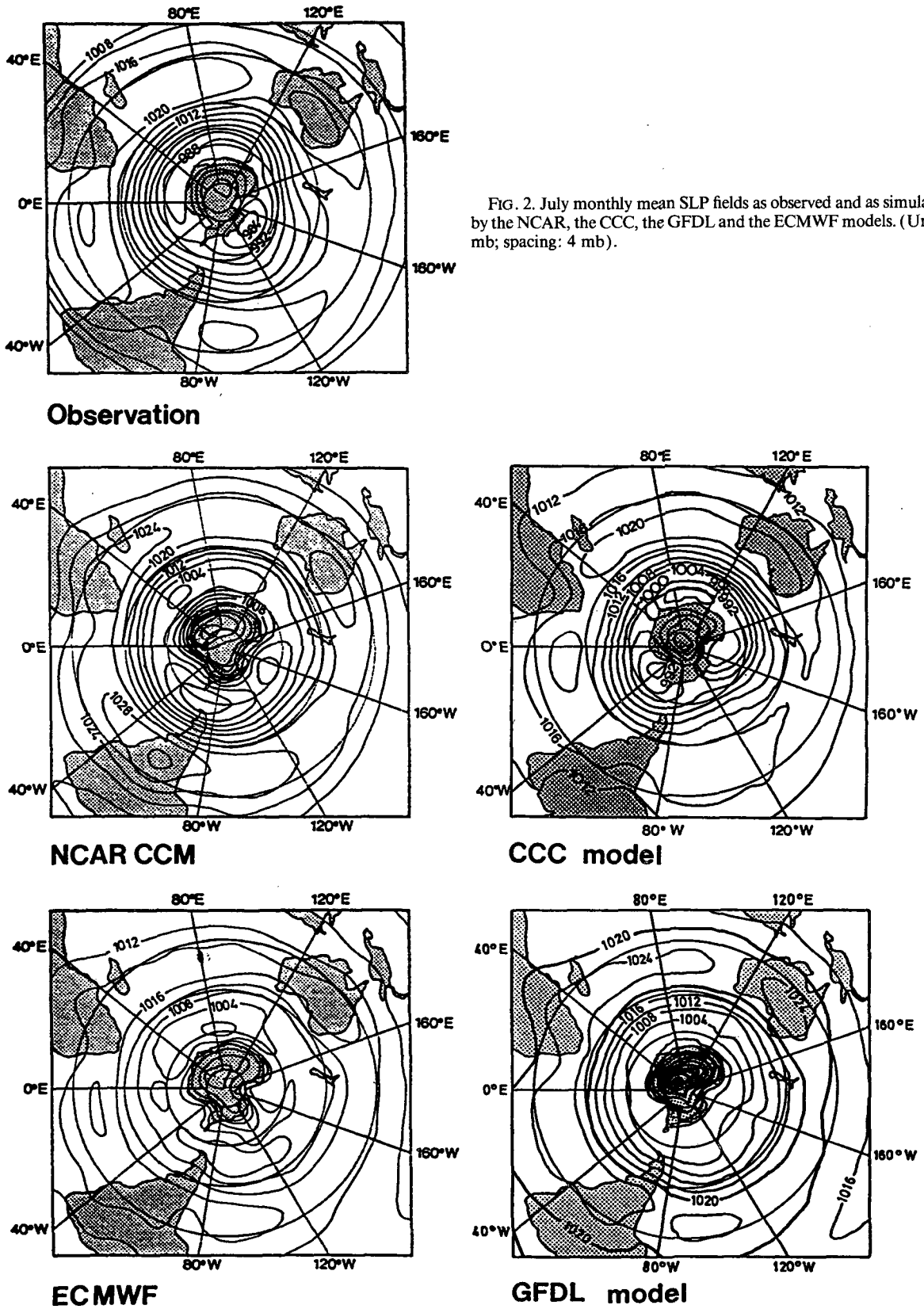

FIG. 2. July monthly mean SLP fields as observed and as simulated by the NCAR, the CCC, the GFDL and the ECMWF models. (Units: mb; spacing: 4 mb).

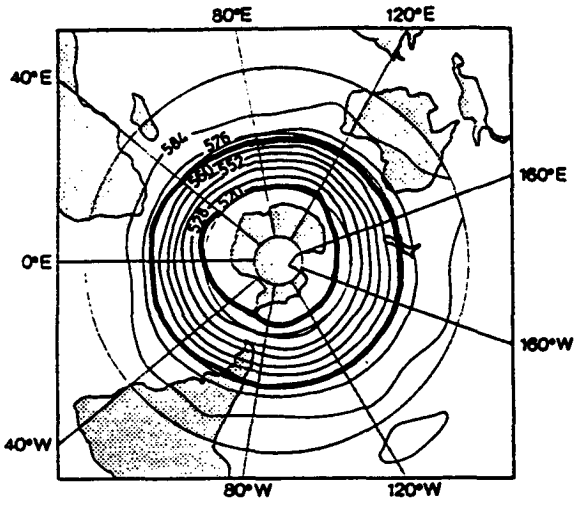

Observation

FIG. 3. January monthly mean 500-mb geopotential height fields as observed and as simulated by the NCAR, the CCC, the GFDL and the ECMWF models. (Spacing: 8 gpdam.) The heavy lines are the isolines closest to 60°S and 40°S, which are shown to help the reader assess the strength of the midlatitude meridional gradient.

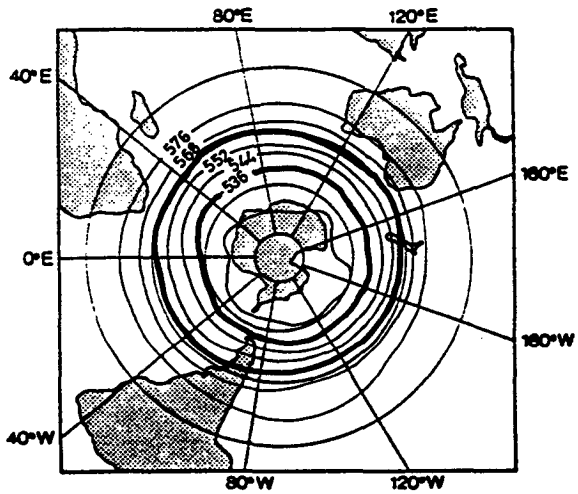

NCAR CCM

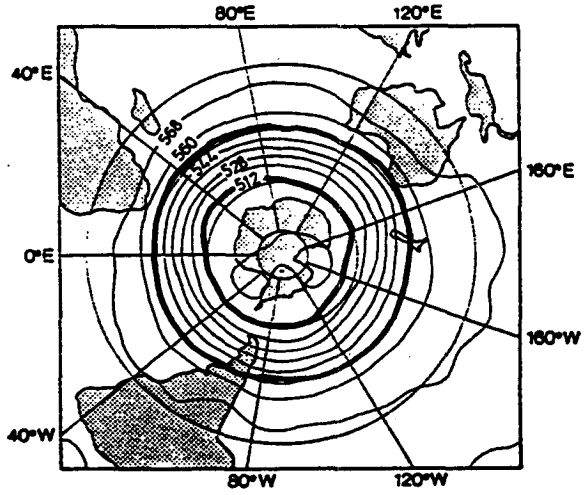

CCC model

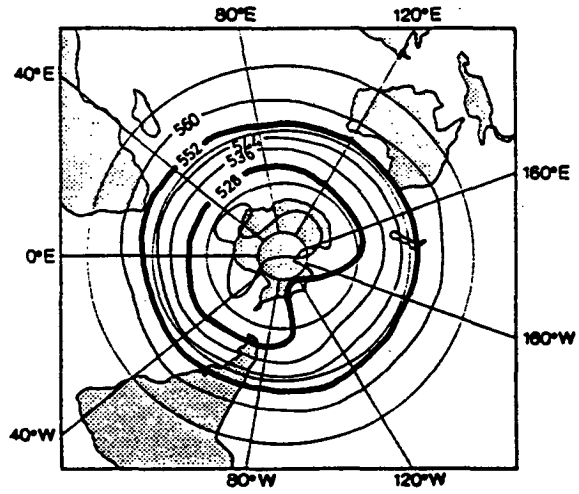

ECMWF

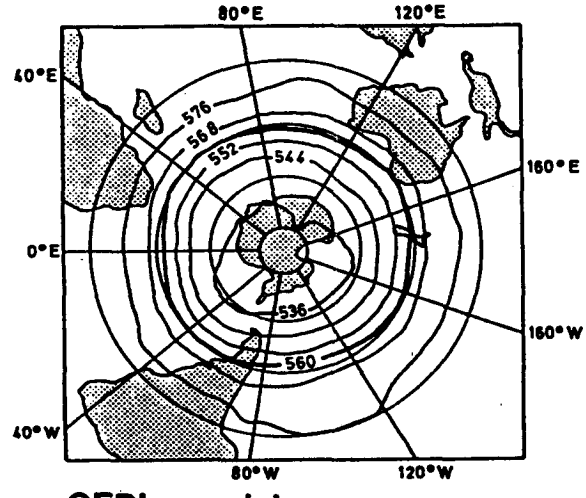

GFDL model

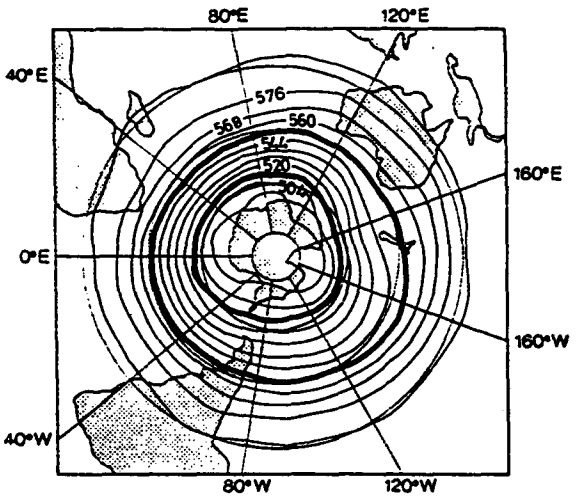

Observation

FIG. 4. July monthly mean 500-mb geopotential height fields as observed and as simulated by the NCAR, the CCC, the GFDL and the ECMWF models. (Spacing: 8 gpdam.) The heavy lines are the isolines closest to 60°S and 40°S that are shown to help the reader assess the strength of the midlatitude meridional gradient.

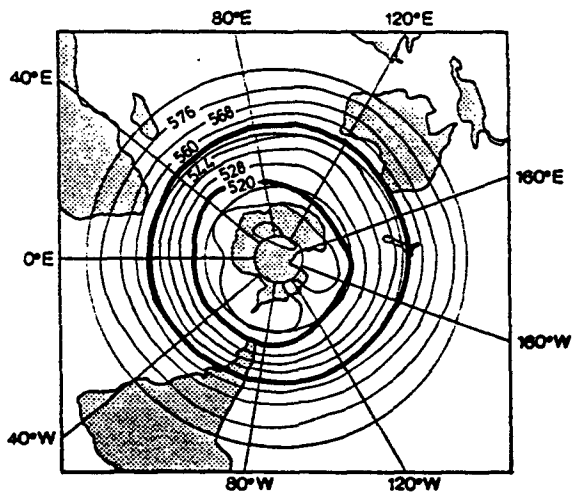

NCAR CCM

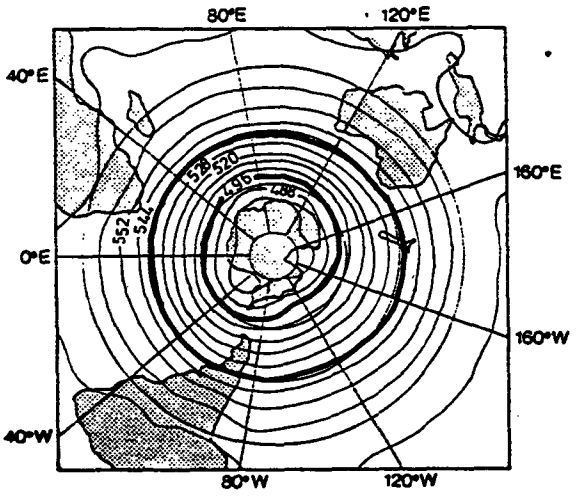

CCC model

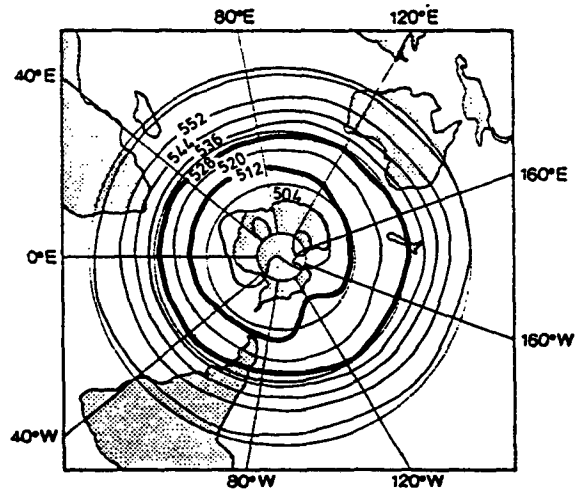

ECMWF

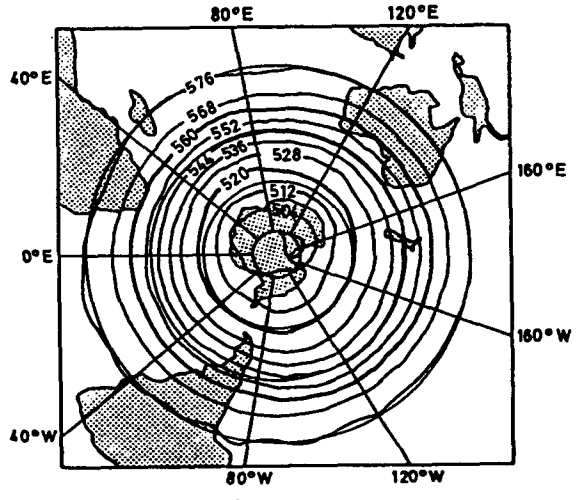

GFDL model

steeper meridional gradient over the eastern than over the western hemisphere.

The mean zonal flow is considerably underestimated in the ECMWF, NCAR CCM and GFDL models. The gradient is 33 gpdam/20° latitude in the NCAR CCM, 28 gpdam/20° latitude in the GFDL, and 21 gpdam/20° latitude in the ECMWF models. These underestimates are due to a lowering of the subtropical pressure surface and a raising of the subpolar pressure surface. An unrealistic ridge is situated over the subpolar Pacific Ocean in the ECMWF model, as in the SLP.

The CCC model is far more successful in simulating the zonally symmetric component (Boer et al. 1984). The circumpolar vortex has a zonally averaged meridional gradient of about 40 gpdam/20° latitude, which is nearly as strong as in the observations. The height level is lower everywhere than that of the observed field. The ECMWF, NCAR CCM, and GFDL models are not able to reproduce the zonal asymmetry in the midlatitude gradient, but the CCC does a credible job.

4) Mean 500-mb geopotential height: July

The circumpolar vortex expands from January to July and has two marked zonal asymmetries in July (Fig. 4): (i) a wave 3 at midlatitudes; and (ii) only one meridional gradient maximum over the Atlantic and Indian oceans, but two over the west Pacific Ocean, one near 25°S and the other at subpolar latitudes (double jet).

The expansion of the circumpolar vortex is found in all the simulated 500-mb geopotential fields (Fig. 4). As at sea level, the ECMWF, the GFDL and the NCAR models have midlatitude meridional gradients that are flatter than observed. Over the subpolar Pacific Ocean there is an unrealistic ridge in the ECMWF model. The CCC model produces a more realistic midlatitude zonal circulation, but the geopotential is everywhere lower than observed.

None of the models reproduces the west Pacific double jet, and the simulations of the waves are generally poor.

b. Stationary Waves at 500 mb

The zonally averaged variance of the quasi-stationary 500-mb height waves, and the contributions to it (given in percent of the total variance) by zonal waves 1, 2, and 3, are shown in Fig. 5 (January) and Fig. 6 (July). The phase of waves 1 (Fig. 7) is given as the longitude of the first ridge east of Greenwich.

The observed Southern Hemisphere stationary waves have been described by van Loon and Jenne (1972), who used the monthly mean maps of Taljaard et al. (1969) and the maps of the IGY; and by Trenberth (1980), who used the 1972–78 Australian Bureau of Meteorology analyses. Our observational results mostly agree with these two papers.

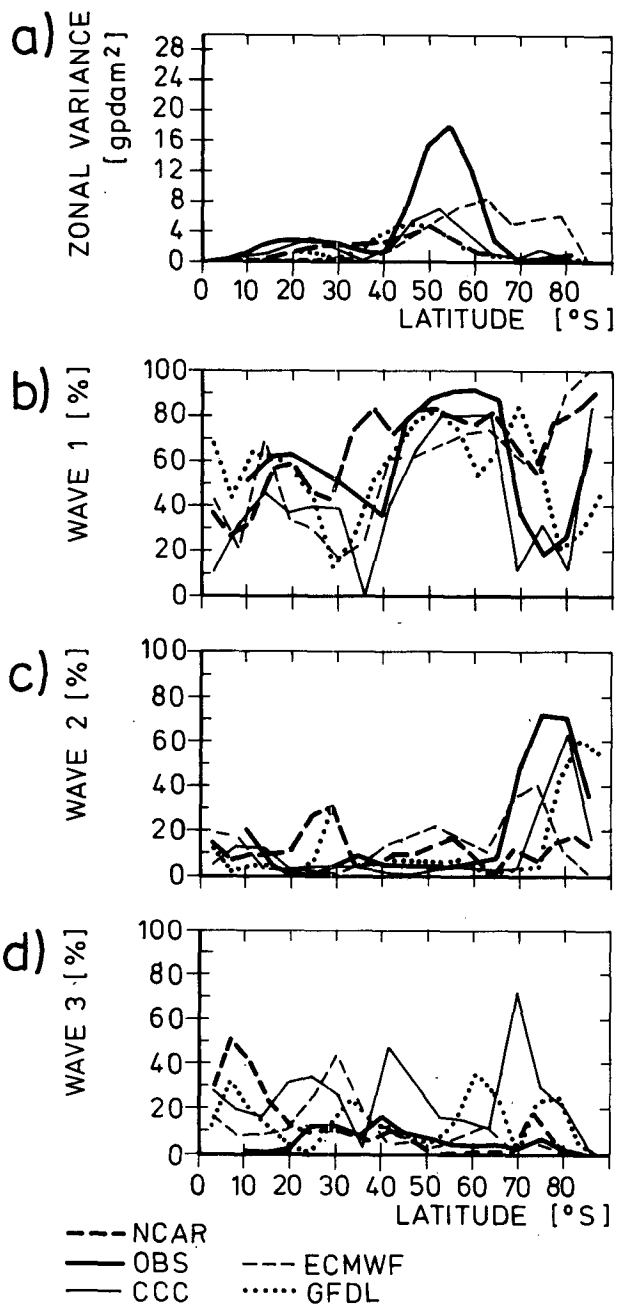

FIG. 5. January mean meridional distributions of (a) zonally averaged variance of the stationary waves, weighted by the cosine of latitude, and (b)–(d) percentage of zonally averaged variance in (a) explained by waves 1, 2 and 3.

1) January

Most of the variance of the observed stationary eddies in January is concentrated at 40°S–65°S (Fig. 5a). Of this variance 80%–90% is due to wave 1 (Fig. 5b), whereas waves 2 and 3 contribute less than 10% each (Figs. 5c, d). Even though the total variance in the secondary maximum north of 40°S is only one-tenth of the maximum values of about 18 gpdam^2 at 55°S

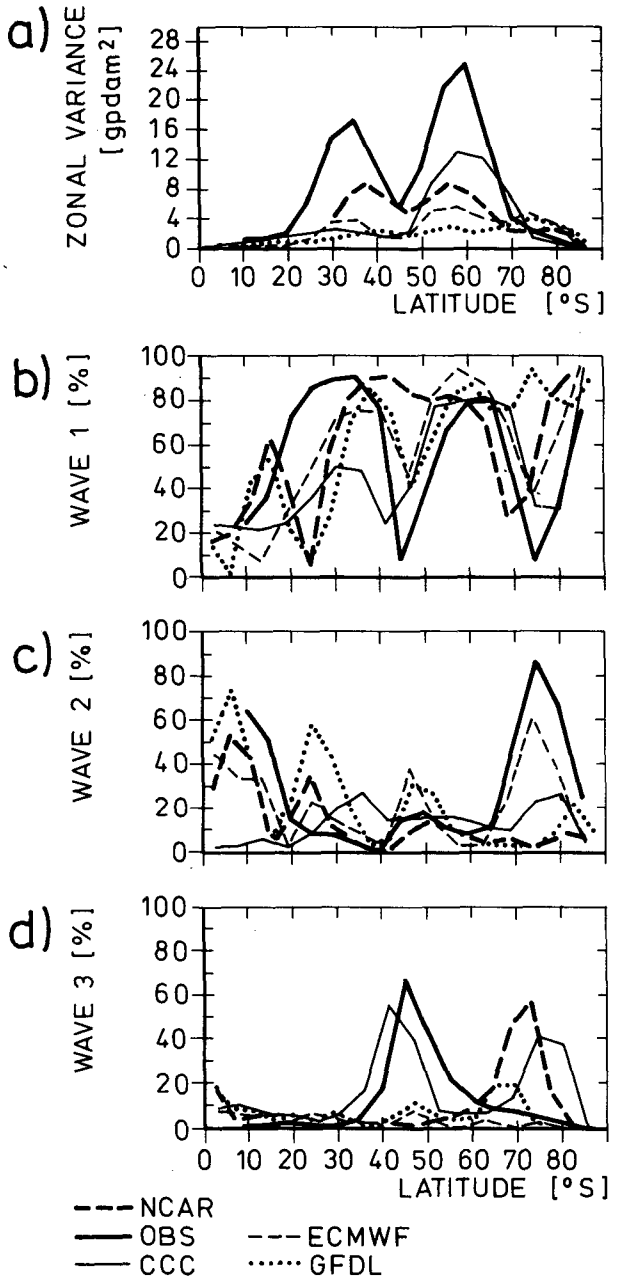

FIG. 6. July mean meridional distributions of (a) the zonally averaged variance of the stationary waves, weighted by the cosine of latitude, and (b)–(d) the percentage of zonally averaged variance in (a) explained by waves 1, 2 and 3.

(Fig. 5a), it is important for the atmospheric circulation in the subtropics and tropics. About 50–60% of the subtropical stationary variance is explained by wave 1, and the remaining 40–50% is mostly connected with wave numbers greater than 3.

The meridional distribution of the position of the ridge of the dominant wave 1 is displayed in Fig. 7a. There is a discontinuity at 40°S where the phase changes. From 40°S to 70°S the ridge is located between 150°W and 120°W. This asymmetry, which also exists in the sea surface temperature south of 40°S and in all tropospheric elements, has been related to the shape of Antarctica (van Loon and Jenne 1972). Equatorward of 40°S the ridge is situated between 10°W and 50°E, which is about 180° away from a trough that is associated with the convectively active area in the South Pacific Convergence Zone.

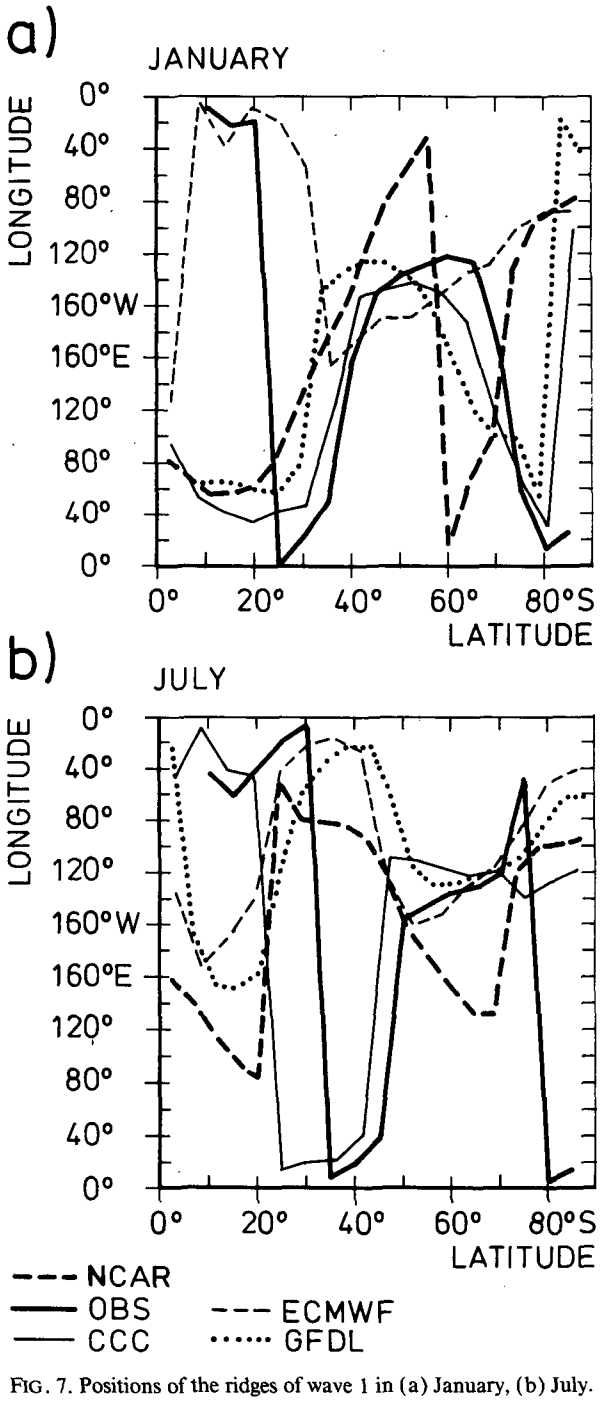

FIG. 7. Positions of the ridges of wave 1 in (a) January, (b) July.

All the models underestimate the level of stationary eddy variance at almost all latitudes (Fig. 5a). The simulated midlatitude variances are less than one-half of the observed value. At subtropical latitudes, the CCC variances have realistic levels. At higher latitudes, the ECMWF GCM overestimates the stationary variance because of the unrealistic ridge in the Pacific mentioned earlier.

Zonal wave 1 contributes most to the maximum of stationary eddy variance at mid- and subpolar latitudes in all GCMs (Fig. 5b), as it does in the observations. Large portions of the variance at mid- and subpolar latitudes are explained by wave 3 in the CCC and the GFDL model (20–60%), and by wave 2 in the ECMWF model and the NCAR CCM (20–25%) (Figs. 5c, d).

The positions of the ridges of wave 1 simulated by the GCMs are shown in Fig. 7a. All the models except for the NCAR CCM generate a zonal wave 1 with a realistic phase at subpolar latitudes. The subpolar zonal wave 1 might, therefore, originate in the CCC and the GFDL models from the same processes as in the atmosphere. In the ECMWF model it is affected by the unrealistic South Pacific ridge.

2) JULY

The level of the observed stationary eddy variance rises almost everywhere in the Southern Hemisphere from summer to winter. In the subtropics this increase is pronounced; at 30°S the January variance is about 3 gpdam^2, but in July about 18 gpdam^2. There is only one large variance maximum in January, but in July Fig. 6a shows two large maxima at about 35°S and 55°–60°S. Both maxima are associated with wave 1, which explains about 90% of the total variance near 35°S and about 80% near 60°S (Fig. 6b). At 45°S where wave 1 changes phase, nearly 70% of the variance is explained by wave 3 (Fig. 6d).

The subtropical wave 1 intensifies strongly from summer to winter with its trough over the west Pacific Ocean (Fig. 7b). Van Loon and Jenne (1972) point out that this location is related to conditions favorable for the formation of cut-off cold lows between 25°S and 30°S in the Australia–New Zealand sector, which are more frequent in this region than anywhere else at these latitudes during the colder part of the year. This situation is associated with a double temperature gradient maximum and related through the thermal wind relation to the double westerly wind maximum. Therefore, the success in generating a correct subtropical zonal wave 1 with its trough over the west Pacific Ocean is an indication of the model's ability to simulate the double jet.

The strong midlatitude wave 3 in July is presumably related to the three low-latitude continents (van Loon and Jenne 1972).

The simulated stationary eddy variance in winter is larger than in summer in all models except for the GFDL model. The simulated overall level of this variance is most often less than 50% of the observed value (Fig. 6a). The underestimation is most severe in the GFDL model.

The ECMWF and NCAR models correctly have two maxima of stationary eddy variance, at middle and subtropical latitudes, but the CCC model has one midlatitude maximum only. All the maxima may be attributed to zonal wave 1 (Fig. 6b). The phase distribution of wave 1 (Fig. 7b) is correctly simulated by the ECMWF, CCC and GFDL models with an abrupt phase change at about 45°S. In the NCAR model, however, the phase changes smoothly. Except for the CCC model, no noticeable midlatitude wave 3 is found in the simulations.

c. Mean 500-mb meridional temperature gradient

The most prominent feature of the Southern Hemisphere summer circulation—i.e., the midlatitude jet stream and its zonal asymmetry (stronger in the Indian Ocean and weaker in the Pacific Ocean)—is through the thermal wind relation directly related to the mean meridional temperature gradient. Similarly, the winter double jet is reflected in the mean meridional temperature gradient. We, therefore, examine this quantity in the observations (Fig. 8) and in the GCM data (not shown).

In the observed mean January temperature field at 500 mb there is a belt of steepest gradient at 40–55°S coinciding with the midlatitude jet stream. In subpolar regions the gradient has a wave 1 asymmetry with maximum values over the Indian Ocean and minimum values over the Pacific Ocean reflecting the zonal asymmetry of the jet stream. The CCC model produces a temperature gradient that is somewhat too steep. The other three GCMs, however, generate gradients flatter than observed, and the zonal circulation is thus too weak in these models. In all the models, the temperature gradient field is too zonally symmetric, which is consistent with the underestimate of the quasi-stationary eddies in the GCMs.

In July, the maximum meridional gradient of observed 500-mb temperature is shifted about 10° northward (35°S–45°S) compared to its summer position and is stronger here than in summer (van Loon 1966). In the Australian–Pacific sector the double maximum of the meridional gradient separated by a midlatitude minimum is connected to the double jet. The models' ability to reproduce the observed wintertime gradients is poor. Though there is a northward displacement of the steepest gradient from summer to winter, only the NCAR and ECMWF models show secondary temperature gradient maxima at subpolar latitudes south of Australia. In the ECMWF model the subpolar trough in the SLP is located too far north, so that only the northernmost westerly wind maximum is reproduced at 500 mb. In the NCAR CCM, besides the problem

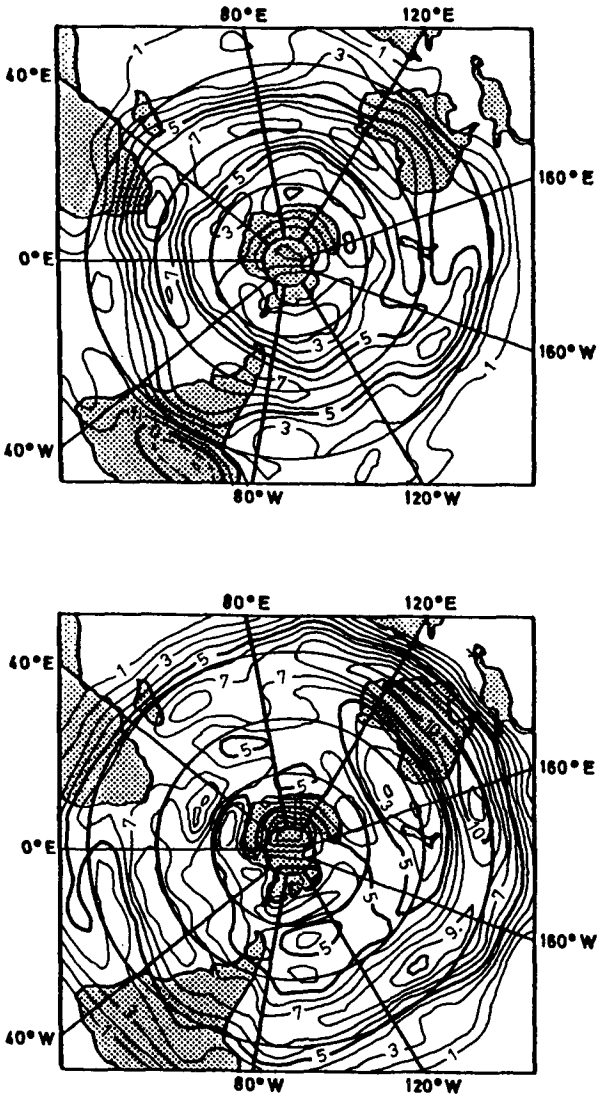

FIG. 8. Observed meridional gradient of 500-mb temperature in January (top) and July (bottom) (Spacing: 1° K/lat).

with the trough, the subtropical temperature gradient maximum lies over the Indian Ocean and South Africa, and, therefore, no west Pacific double jet is produced by this model. Generally the ECMWF model simulates a realistic subtropical circulation, but it has a number of serious problems at mid- and high latitudes.

4. Extratropical semi-annual wave

a. Semi-annual wave in the SLP field

The amplitude and phase of the half-yearly SLP wave and the percentage of the annual variance explained by the half-yearly wave are shown in Fig. 9 for the observed data; in Fig. 10 for the CCC model; in Fig. 11 for the NCAR CCM; in Fig. 12 for the GFDL model; and in Fig. 13 for the ECMWF model. The phase is defined as the date of the first maximum.

The observed extratropical semiannual wave has a large amplitude and explained variance at middle and high latitudes (van Loon 1967, 1972). The amplitude and variance minimum along 60°S is connected with a phase reversal from maxima in the transitional seasons to the north to maxima in the extreme seasons to the south. At midlatitudes in the center of each ocean and at high latitudes, the explained variance is larger than 50%, locally it is larger than 80%.

The semiannual wave is underestimated or not correctly reproduced by the models considered here. The GFDL model (Fig. 12) and the NCAR CCM (Fig. 12) models produce a semiannual wave that resembles the actual one in middle and high latitudes. The GFDL semiannual wave has three maxima of amplitude and explained variance at midlatitudes over oceans, with peaks in February/March, and at high latitudes with peaks in January. In the NCAR CCM the semiannual wave is fairly realistically simulated over the Pacific Ocean.

b. The semi-annual wave in the 500-mb temperature gradient

We have shown that the GCMs have different mean states in the Southern Hemisphere. In addition, the extratropical semiannual waves simulated by the models are unrealistic or too weak. Why do the models fail to simulate correctly the extratropical semiannual wave in the Southern Hemisphere?

According to van Loon (1967), the semiannual wave in the SLP is associated with the different shape of the annual curves of sea surface and tropospheric temperature in oceanic middle and continental high latitudes. These differences appear in the troposphere as a semiannual wave in the meridional temperature gradient that has maxima in the transitional seasons at midlatitudes. Because changes of the meridional temperature gradient represent changes of baroclinity, the semiannual variation of the temperature gradient is associated with a semiannual variation of cyclonic activity, and thus of the mean SLP.

To test this observation on the model climatologies, the semiannual variation of the intensity and position of the subpolar trough, and in the temperature gradient at 500-mb, was calculated from observations and from the four GCMs' climatologies. In the observed 500-mb meridional temperature gradient (Fig. 14) the semiannual wave is strong near 55°S and near 35°S. In the southernmost belt, where the second harmonic peaks in the transition months, the amplitude is larger than 10×10^{-2} K/° lat and the largest values are 16×10^{-2} K/° lat, which explains 30–80% of the total variance. In the semiannual wave along 35°S the peaks are in the extreme season. The harmonic here explains 20–40% of the annual variance.

At the surface, the annual variation of the zonally averaged intensity and position of the subpolar trough

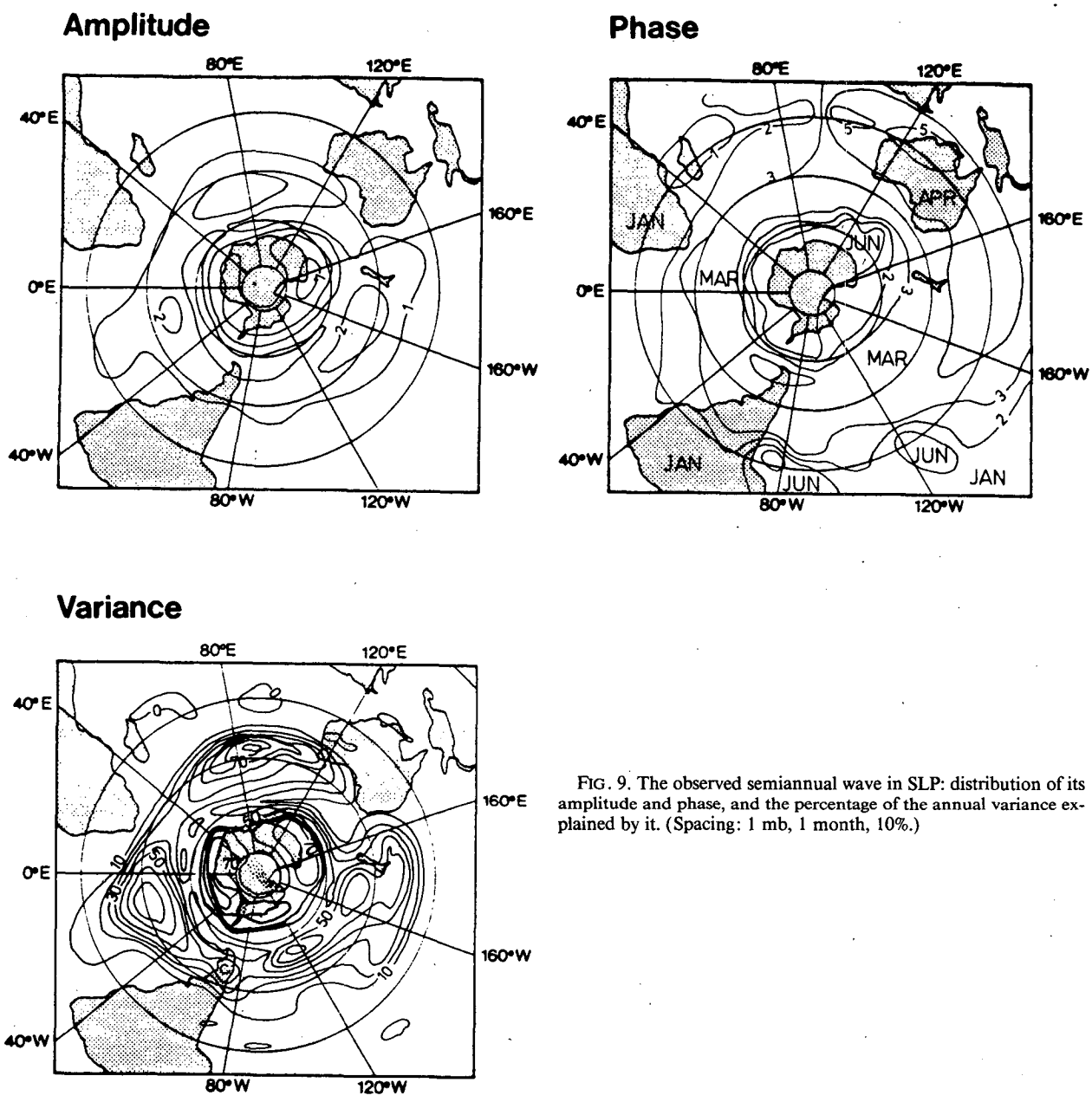

FIG. 9. The observed semiannual wave in SLP: distribution of its amplitude and phase, and the percentage of the annual variance explained by it. (Spacing: 1 mb, 1 month, 10%.)

is dominated by a semiannual wave, which explains 76% (intensity) and 60% (position) of the mean annual variance (Fig. 15). The trough is most intense and farthest south in the transitional seasons when the 500 mb temperature gradient at 55°S is at its maximum, but farthest north in the extreme seasons when the temperature gradient at 35°S is strongest.

The semiannual wave in 500-mb temperature gradient is too weak in all the models (not shown). In the GFDL model the southernmost belt extends as far north as 40°S and peaks in March/April, and the northernmost belt peaks in January/February. Both are too weak with an amplitude of about 2–4 $\times$ (10^{-2} K/° lat). In the NCAR CCM the semiannual wave over the west Pacific Ocean resembles the observations with one amplitude maximum at 55°S, peaking in March/September, and another at 35°S, peaking in June/December. Outside the west Pacific, however, the NCAR model fails to reproduce the observed pattern of two belts that are out-of-phase. This characteristic pattern is nowhere reproduced by the CCC and ECMWF models.

The annual march of the position and the strength of the zonally averaged subpolar trough in the four

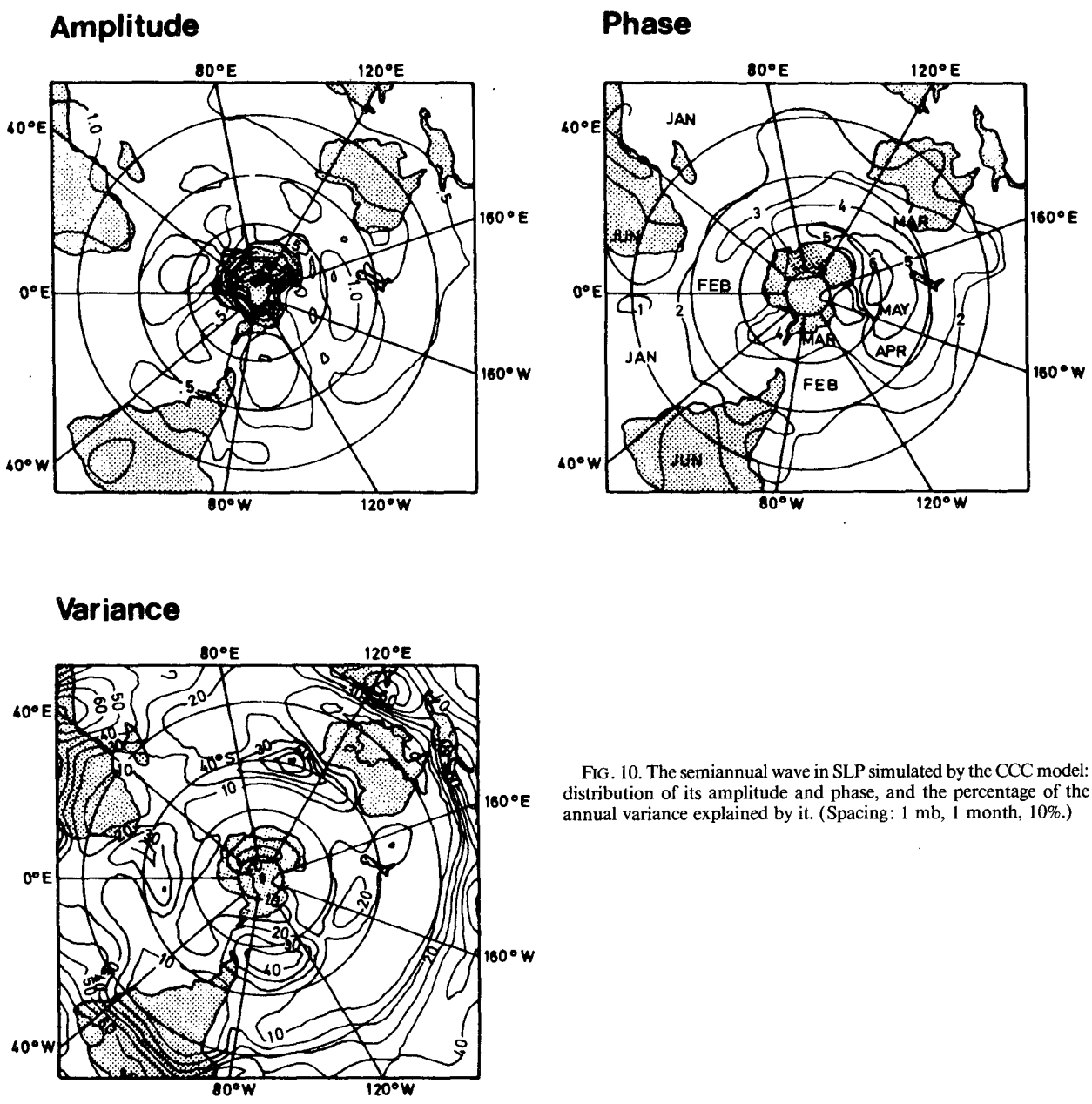

FIG. 10. The semiannual wave in SLP simulated by the CCC model: distribution of its amplitude and phase, and the percentage of the annual variance explained by it. (Spacing: 1 mb, 1 month, 10%.)

models is shown in Fig. 15. In both the CCC and ECMWF models the trough is completely dominated by the annual harmonic. In contrast to the observations, the troughs of these models are most intense and farthest south in summer. The annual marches of the temperature gradient simulated by the CCC and the ECMWF model, however, agree with the observations with maxima in winter (not shown). The NCAR and the GFDL models are slightly more realistic with respect to the shape of the annual curve of the intensity, but the trough is too weak and mostly lies too far north in both cases.

5. Summary and discussion

We examined the ability of four low-resolution spectral GCMs to reproduce the mean winter and summer circulations on the Southern Hemisphere and to produce a realistic semiannual wave at middle and high latitudes. The models' skill to do so is generally poor. Because the models considered vary with respect to various aspects of their numerical details and the parameterization of subgrid scale physical processes, no easy answer about why the models behave differently is possible.

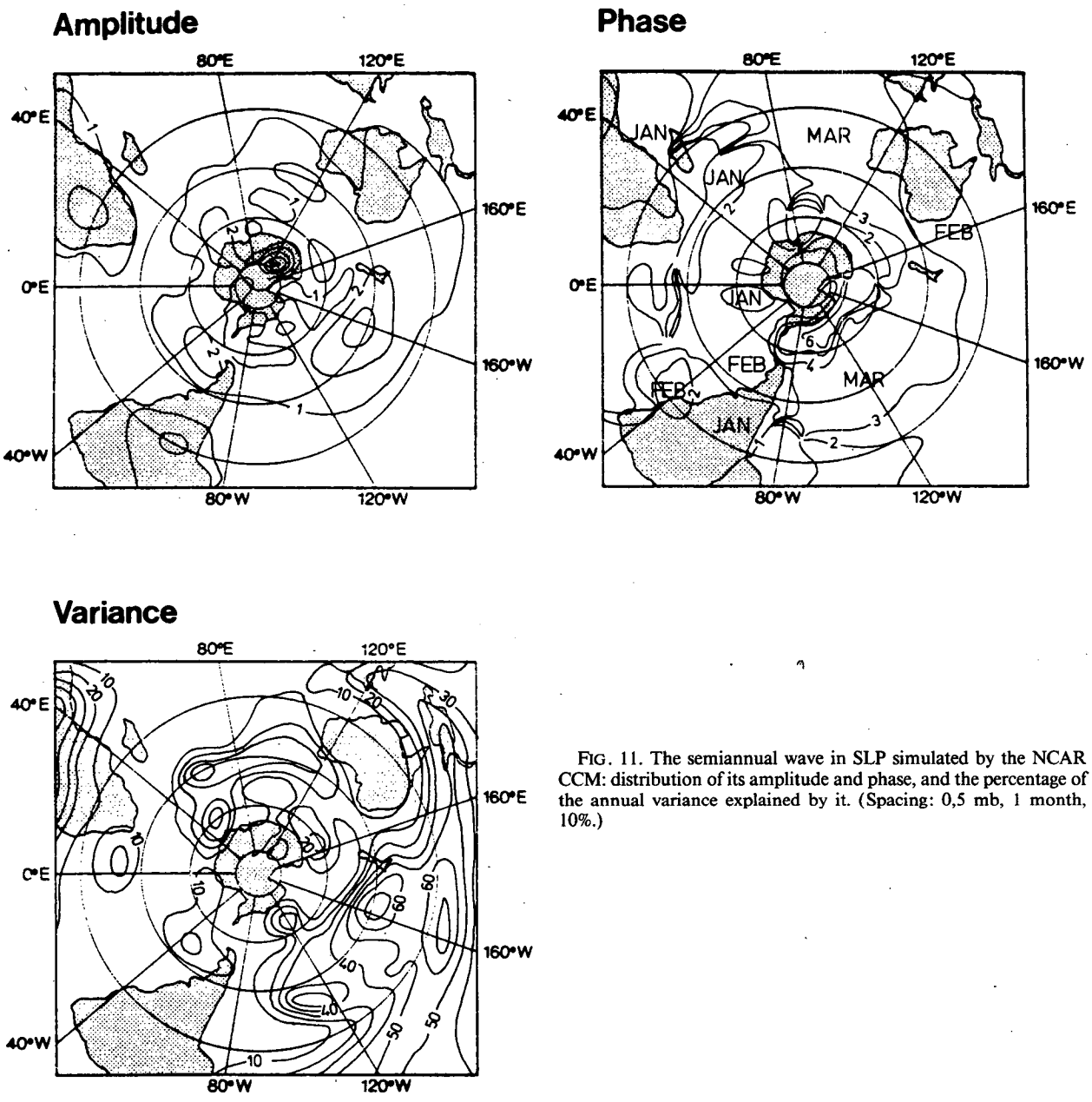

FIG. 11. The semiannual wave in SLP simulated by the NCAR CCM: distribution of its amplitude and phase, and the percentage of the annual variance explained by it. (Spacing: 0,5 mb, 1 month, 10%.)

a. The zonally symmetric flow

The observations of SLP are characterized by a subtropical ridge, a strong midlatitude gradient and a subpolar trough. All the models are fairly successful in reproducing the subtropical ridge, but all models, except the CCC model, underestimate the midlatitude gradient and produce a subpolar trough that is too weak and lies too far north. In the CCC model, the midlatitude gradient and the subpolar trough look realistic, but the trough is not in phase with the observed annual march of the 500-mb temperature gradient, which indicates that the relatively realistic results might occur for the wrong reasons.

When comparing our results with the performance of other models reported in the literature, we find that most models are capable of simulating the subtropical ridge. With respect to the midlatitude gradient, the ECMWF model scores worst in our study, but interestingly there are models which behave even more poorly (the GISS and the GLAS model, see Schlesinger 1984a). Some grid-point models, however, have a steep midlatitude gradient; e.g., the OSU and the UCLA model (Schlesinger) or the MRI-GCM-I (Tokioka et

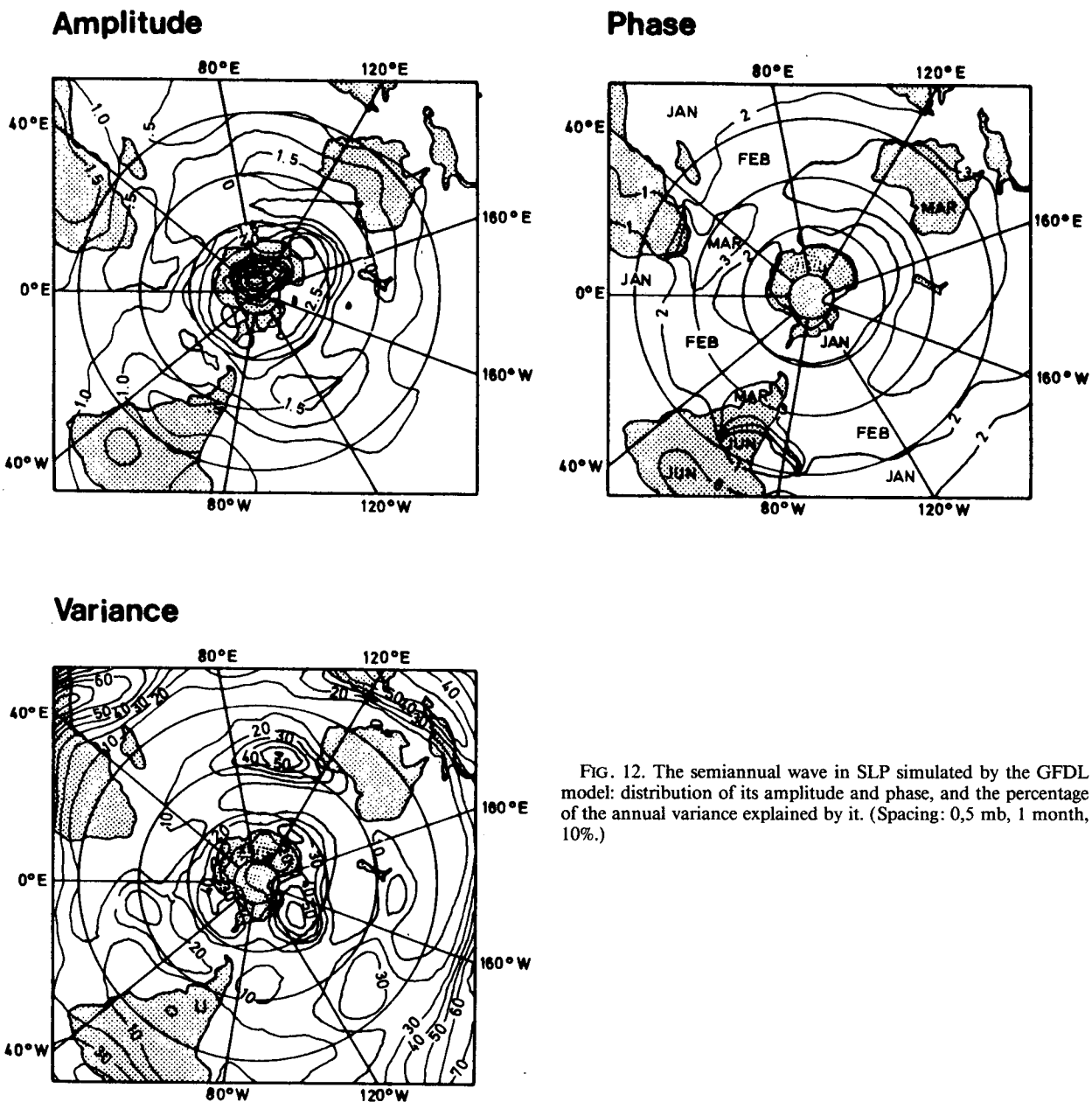

FIG. 12. The semiannual wave in SLP simulated by the GFDL model: distribution of its amplitude and phase, and the percentage of the annual variance explained by it. (Spacing: 0,5 mb, 1 month, 10%.)

al. 1985; Kitoh 1986). The spectral R15 model of the Australian Bureau of Meteorology also has a much too flat midlatitude gradient (Hart et al. 1988).

It is sometimes said that spectral models would perform better on the Southern Hemisphere if the resolution were increased. This question was examined in some detail in the BMRC model (Hart et al. 1988; their Fig. 16). When increasing the resolution from R15 to R21 and R31, they found a steeper midlatitude Southern Hemisphere gradient. At the same time, however, the Northern Hemisphere midlatitude gradient, which was well described by the R15 model, also became steeper. In the CCC model, an increase of the horizontal resolution from T20 to T30 and T40 did lead to minor changes of the Southern Hemisphere mean circulation (Boer and Lazare 1988).

b. Zonal asymmetries

All GCMs considered here underestimate the variance of the stationary eddies. In summer the zonal asymmetries are strongest at midlatitudes and are explained mainly by wave 1. The four models generate a zonal wave 1, and except for the NCAR CCM the

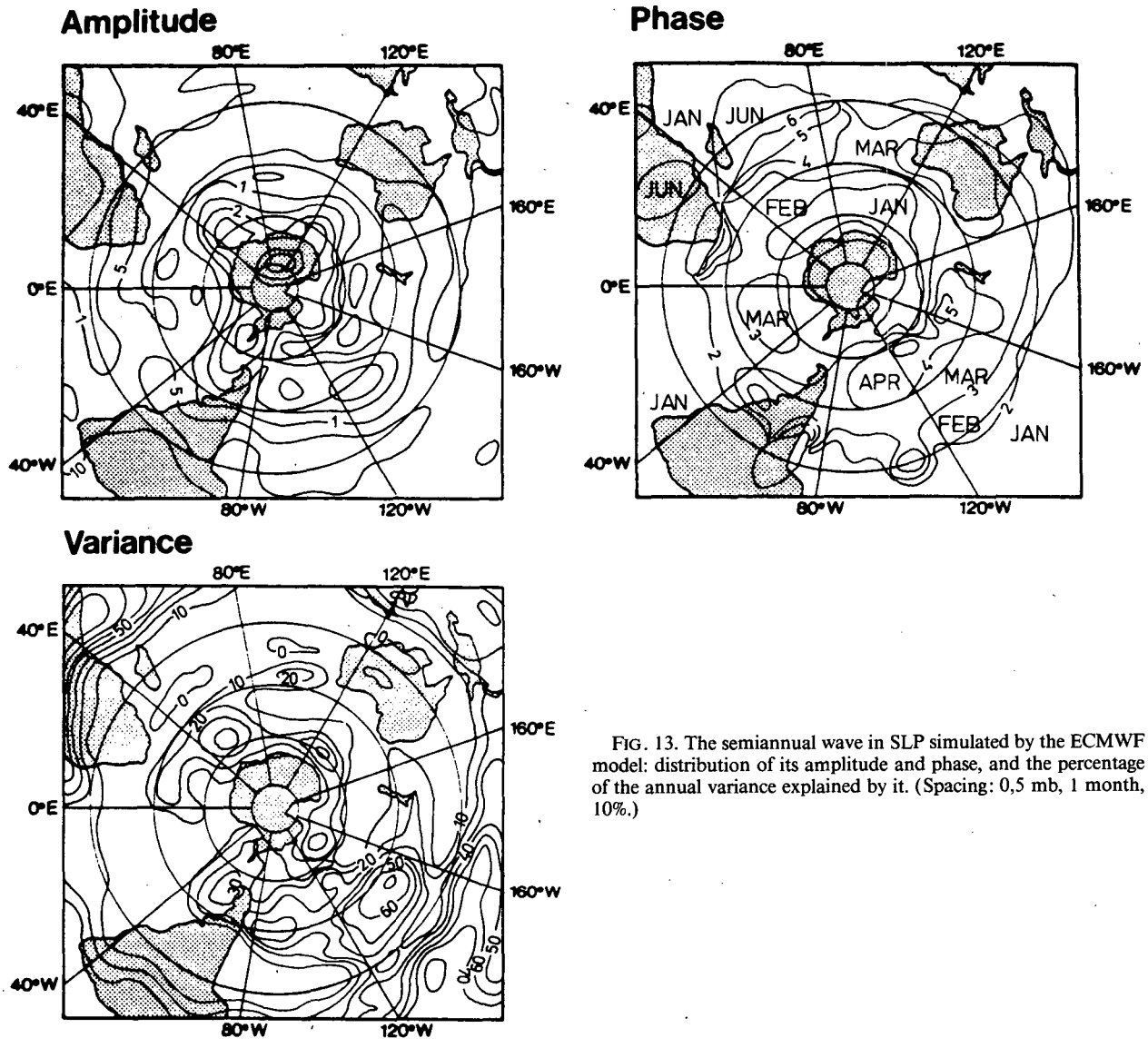

FIG. 13. The semiannual wave in SLP simulated by the ECMWF model: distribution of its amplitude and phase, and the percentage of the annual variance explained by it. (Spacing: 0,5 mb, 1 month, 10%.)

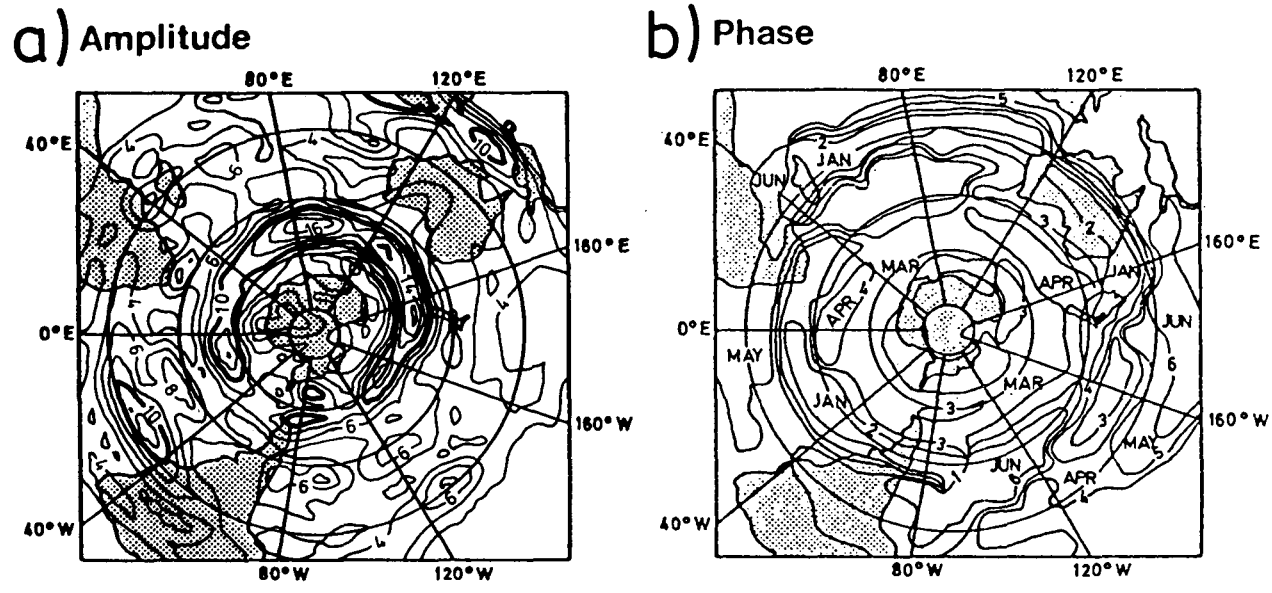

FIG. 14. The observed semiannual wave in 500-mb meridional temperature gradient: distribution of its amplitude and phase (Spacing: 2×10^{-2} K/°lat, 1 month).

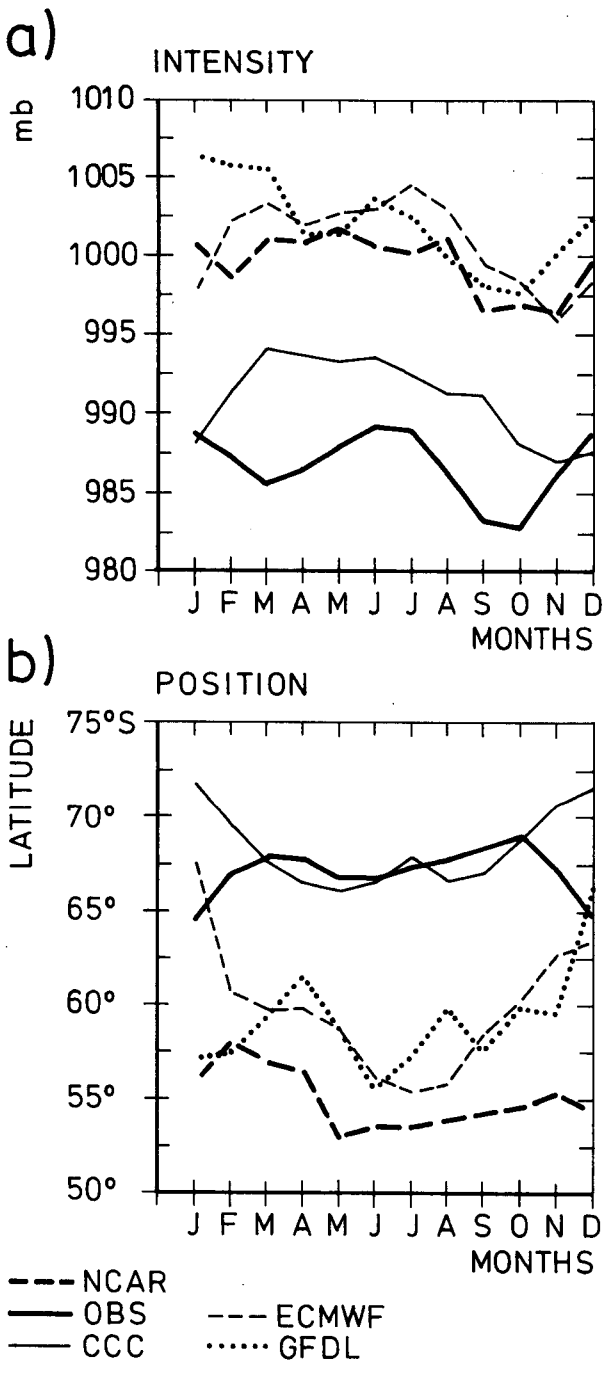

FIG. 15. The annual march of the zonally averaged a) intensity (mb) and b) the position (°S) of the subpolar trough in the observations, the CCC model, the NCAR CCM, the GFDL model, and the ECMWF model.

wave is fairly realistic. In winter, the observed zonal variance of the quasi-stationary waves is larger than in summer. Two maxima are present, one at subtropical latitudes and the other at subpolar latitudes. Both are dominated by wave 1, which reverses phase near 40°S, and these height anomalies are associated with a double jet stream in the Australia–Pacific sector. Only the ECMWF model has some success in reproducing the subtropical wave 1.

c. *Semiannual wave*

All models considered generate an unrealistic and much too weak semiannual wave in both the sea level pressure and in the 500-mb temperature gradient. The fact that all the GCMs, except possibly the GFDL model, fail to simulate the correct spatial distribution of the phase and amplitude of the semiannual wave indicates that the models' semiannual wave might be mostly model noise.

d. *Conclusion*

Both the winter double jet and the semiannual variation of sea level pressure are reflected in the meridional gradient of the tropospheric temperature. This tropospheric gradient is associated with differences in the seasonal heating and cooling of land, ocean and ice. The GCMs' inability to simulate the winter double jet and the semiannual variation is thus indicative of an inadequate thermal coupling between the surface and the troposphere in the four models. We suggest that the models' deficiencies are mostly due to insufficient parameterizations of subgrid scale physical processes. The sensitivity of the Southern Hemisphere circulation to changes of parameterizations was impressively demonstrated by Meehl and Albrecht (1988) who used different formulations of (mostly tropical) convection.

Acknowledgments. We wish to thank F. W. Zwiers and G. Boer from the Canadian Climate Centre, G. A. Meehl from NCAR, N. C. Lau from GFDL and the staff of the Meteorological Institute of Hamburg University, who provided us with the GCM data. We are indebted to Mrs. Grunert, Mrs. Lewandowski, and Mrs. Meyer-Wildenhofer for preparing the diagrams.

REFERENCES

Boer, G. J., N. A. McFarlane and R. Laprise, 1984: The climatology of the Canadian Climate Centre General Circulation Model as obtained from a five-year simulation. *Atmos.-Ocean,* **22,** 430–473.

——, and M. Lazare, 1988: Some results concerning the effect of horizontal resolution and gravity-wave drag on simulated climate. *J. Climate,* **1,** 789–806.

Fischer, G. (Ed.), 1987: Climate Simulations with the ECMWF ECMWF-model in Hamburg. *Large Scale Modelling Report 1,* Meteorologisches Institut der Universität Hamburg, Bundesstraße 55, 2000 Hamburg 13, FR Germany.

Gordon, C. T., and W. F. Stern, 1982: A description of the GFDL global spectral model. *Mon. Wea. Rev.,* **110,** 625–644.

Hart, T. L., W. Bourke, B. J. McAvaney, B. W. Forgan and J. L. McGregor, 1988: Atmospheric general circulation simulations with the BMRC global spectral model: the impact of revised physical parameterizations. *BMRC Research Report 12,* Bureau of Meteorology Research Centre, GPO Box 1289K, Melbourne, Victoria, Australia 3001.

Kitoh, A., and T. Tokioka, 1986: A simulation of the tropospheric general circulation with the MRI general circulation model. Part II: The July performance. *Papers in Meteorology and Geophysics,* **37,** 145–168.

Manabe, S., and D. G. Hahn, 1981: Simulation of atmospheric variability. *Mon. Wea. Rev.,* **109,** 2260–2286.

Meehl, G. A., 1989: The coupled ocean–atmosphere modeling problem in the tropical Pacific and Asian monsoon region. *J. Climate,* in press.

——, and B. A. Albrecht, 1988: Tropospheric temperatures and Southern Hemisphere circulation, *Mon. Wea. Rev.,* **116,** 953–960.

Schlesinger, M., 1984a: Atmospheric general circulation model simulations of the modern Antarctic climate. *Environment of West Antartica;* Committee on Glaciology of the Polar Research Board, Commission of Physical Sciences, Mathematics and Resources, National Science Council, National Academy Press, Washington D.C., 155–196.

——, 1984b: Atmospheric general circulation model simulations of the modern Antarctic climate. *Proceedings of the 9th Climate Diagnostics Workshop,* Oregon State University, 22–26 October, 201–210 [NTTS PB85-183911].

Taljaard, J. J., H. van Loon, H. L. Crutcher and R. L. Jenne, 1969: *Climate of the Upper Air: Southern Hemisphere I.* NAVAIR 50-IC-55, Chief of Naval Ops, Washington DC, 135 pp.

Tokioka, T., A. Kitoh, I. Yagai and K. Yamazaki, 1985: A simulation of the tropospheric general circulation with the MRI atmospheric general circulation model. Part I: The January performance. *J. Met. Soc. Japan,* **63,** 749–778.

Trenberth, K. E., 1980: Planetary waves at 500-mb in the Southern Hemisphere. *Mon. Wea. Rev.,* **108,** 1378–1389.

van Loon, H., 1966: On the annual temperature range over the southern oceans. *Geograph. Rev.,* **56,** 497–515.

——, 1967: The half-yearly oscillations in middle and high southern latitudes and the coreless winter. *J. Atmos. Sci.,* **24,** 472–486.

——, 1972: Pressure in the Southern Hemisphere. *Meteorology of the Southern Hemisphere,* Ed., C. W. Newton, *Meteor. Monogr.* No. 35, Amer. Meteor. Soc. 35, 87–100.

——, and R. L. Jenne, 1972: The zonal harmonic standing waves in the Southern Hemisphere. *J. Geophys. Res.,* **77,** 992–1003.

——, and J. C. Rogers, 1984: Interannual variations in the half-yearly cycle of pressure gradients and zonal wind at sea level on the Southern Hemisphere. *Tellus,* **36A,** 76–86.

von Storch, H., and J. Xu, 1987: Southern Hemisphere: Comparison with observed sea level pressure. Climate Simulations with the ECMWF T21 model in Hamburg, *Large Scale Modelling Report 1,* G. Fischer (Ed.), Meteorologisches Institut der Universität Hamburg, Bundesstraße 55, 2000 Hamburg 13, FR Germany, 57–73.

Washington, W. M., and G. A. Meehl, 1984: Seasonal cycle experiment on the climate sensitivity due to a coupling of CO_2 with an atmospheric general circulation model coupled to a simple mixed layer ocean model. *J. Geophys. Res.* **89,** 9475–9503.

Weickmann, K. M., and R. M. Chervin, 1988: The observed and simulated atmospheric seasonal cycle I: Global Wind Field Modes. *J. Climate,* **1,** 265–289.